MEDICAL ROBOTS

Magnetically actuated microrobots as a platform for stem cell transplantation

Sungwoong Jeon[1,2]*, Sangwon Kim[3]*, Shinwon Ha[4], Seungmin Lee[1,2], Eunhee Kim[1,2], So Yeun Kim[4], Sun Hwa Park[5], Jung Ho Jeon[5], Sung Won Kim[5,6], Cheil Moon[4], Bradley J. Nelson[1,2,3], Jin-young Kim[1,2†‡], Seong-Woon Yu[4†‡], Hongsoo Choi[1,2†‡]

Magnetic microrobots were developed for three-dimensional culture and the precise delivery of stem cells in vitro, ex vivo, and in vivo. Hippocampal neural stem cells attached to the microrobots proliferated and differentiated into astrocytes, oligodendrocytes, and neurons. Moreover, microrobots were used to transport colorectal carcinoma cancer cells to tumor microtissue in a body-on-a-chip, which comprised an in vitro liver-tumor microorgan network. The microrobots were also controlled in a mouse brain slice and rat brain blood vessel. Last, microrobots carrying mesenchymal stem cells derived from human nose were manipulated inside the intraperitoneal cavity of a nude mouse. The results indicate the potential of microrobots for the culture and delivery of stem cells.

INTRODUCTION

Stem cell therapy has emerged as a promising method for restoring damaged tissues or organs; for example, the use of neural stem cells (NSCs) or neural cells differentiated from stem cells has been considered for the treatment of degenerative neural disorders, such as Alzheimer's disease (*1*, *2*). Numerous types of stem cells, which can be embryonic, adult, or induced pluripotent, are available from various sources (*3*, *4*). Extensive progress has recently been made in stem cell biology and regenerative medicine, demonstrating the potential of stem cell technology for treatment of a wide variety of diseases, ranging from developmental and pediatric diseases to metabolic diseases, cancer, and ischemia, as well as age-related degenerative diseases (*5*–*7*). Stem cell therapy requires the precise delivery of cells to the target tissue. Magnetically actuated microrobots facilitate stem cell transplantation in fluidic environments and can be used for biomedical applications, such as neural interfaces and cell/drug delivery (*8*–*13*). Because of their small size and wireless control by, for example, magnetic fields (*11*–*17*), microrobots have several advantages as medical treatments, such as reduced pain, risk of infection, and trauma. Microrobots with various magnetic field control systems that enable the accurate and efficient locomotion in physiological fluids have been developed (*15*, *18*–*36*).

Cell delivery using different microrobots has been reported in in vivo and in vitro environments (*37*–*39*). The microrobots were designed for the target cells and controlled by external magnetic fields. Magnetic actuation of microrobots is generally used for biomedical applications because it is harmless and undergoes little distortion or attenuation in the body. A capsule-type microrobot is capable of performing pick-up-and-drop motions to deliver olfactory receptor neuron cells adherent to the scaffold-type cap of the microrobot on a rat brain slice (*37*). Porous cubical and burr-like spherical microrobots were manipulated using a magnetic field gradient of 20 T/m; the microrobots transported cells to a targeted area within the transparent yolk of a zebrafish embryo and released the cells in vivo (*38*). A magnetically actuated microstructure was used to deliver mesenchymal stem cells (MSCs) into a microfluidic channel loaded with cells and a three-dimensional (3D) knee joint phantom without cells. A magnetic field gradient of 1.8 T/m was used for articular cartilage regeneration (*39*). In our previous study (*15*), we cultured and delivered human embryonic kidney 293 cells using cylindrical and hexahedral scaffold microrobots controlled by a magnetic field gradient. However, the manipulation of the cylindrical and hexahedral scaffold microrobots by magnetic pulling using the gradient field was not optimized. In addition, most previous studies have used 2D cell culture and did not load a sufficient number of cells onto the microrobot (*24*, *38*); these issues may be overcome by 3D cell culture. In addition, a rotating magnetic field may induce more efficient and controllable motion of microrobots in a confined in vivo fluidic environment.

Here, we show that microrobots facilitated the precise targeting of transplanted stem cells. We developed biocompatible porous 3D microrobots and assessed their feasibility for 3D culture and delivery of stem cells using magnetic locomotion. The spherical and helical microrobots, which exhibited rolling and corkscrew motions upon application of a rotating magnetic field, showed higher propulsion efficiencies than those pulled by a magnetic field gradient. The attachment, proliferation, and differentiation of hippocampal NSCs on the microrobots were confirmed by immunofluorescence staining and scanning electron microscopy (SEM). The application of an external magnetic field enabled the microrobots to be moved to a target location in a body-on-a chip (BoC) microfluidic cell culture platform (in vitro liver-tumor microorgan network), in a ventricle of mouse brain slice (ex vivo), in a rat brain blood vessel (ex vivo), and in a live nude mouse (in vivo). These results demonstrate the feasibility of using microrobots for targeted stem cell transportation and transplantation in various in vitro, ex vivo, and in vivo physiological fluidic environments.

RESULTS

Fabrication and characterization of the microrobots

We designed and fabricated the microrobots using 3D microelectromechanical systems (MEMS) technologies. Figure 1A shows an image of a microrobot with attached cells and a magnetic manipulator. Microrobot fabrication is described in Fig. 1B (details are available in the

---

[1]Department of Robotics Engineering, Daegu Gyeongbuk Institute of Science & Technology (DGIST), Daegu 42988, South Korea. [2]DGIST-ETH Microrobotics Research Center, DGIST, Daegu 42988, South Korea. [3]Institute of Robotic and Intelligent System (IRIS), ETH, Zurich 8092, Switzerland. [4]Department of Brain and Cognitive Sciences, DGIST, Daegu 42988, South Korea. [5]Postech-Catholic Biomedical Engineering Institute, College of Medicine, The Catholic University of Korea, Seoul, South Korea. [6]Department of Otolaryngology-Head and Neck Surgery, Seoul St. Mary's Hospital, The Catholic University of Korea, Seoul 06591, South Korea.
*These authors contributed equally to this work.
†These authors contributed equally to this work.
‡Corresponding author. Email: mems@dgist.ac.kr (H.C.); yusw@dgist.ac.kr (S.-W.Y.); jy.kim@dgist.ac.kr (J.-y.K.)

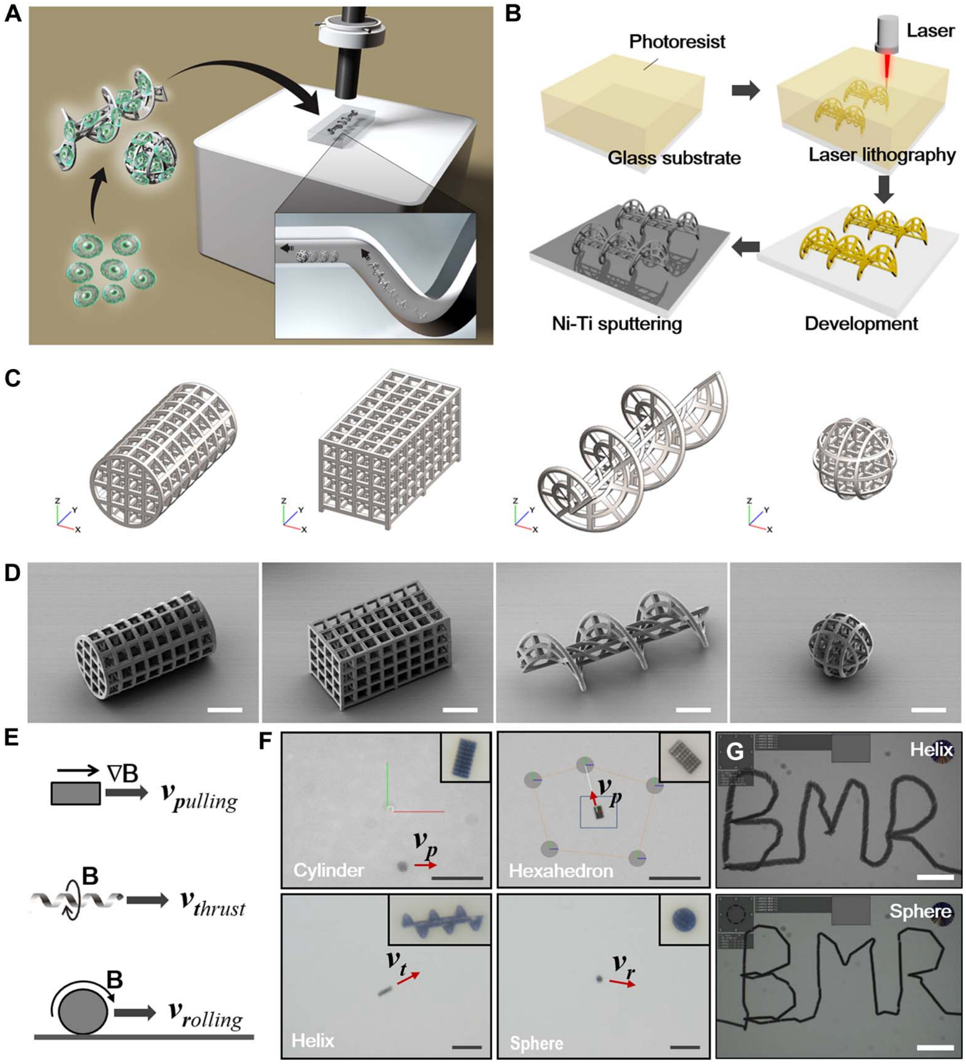

Fig. 1. Fabrication and magnetic actuation of the microrobots. (**A**) Schematic of the microrobots. (**B**) Overall fabrication process of the microrobots. (**C**) CAD layouts for cylindrical, hexahedral, helical, and spherical scaffold-type microrobots. (**D**) SEM images of the fabricated cylindrical, hexahedral, helical, and spherical microrobots. Scale bars, 40 μm. (**E**) The three propulsion mechanisms of the microrobots. (**F**) Cylindrical and hexahedral microrobots pulled by a magnetic field gradient. Helical and spherical microrobots manipulated by a rotating magnetic field. Scale bars, 500 μm. (**G**) Writing of BMR trajectories using helical and spherical microrobots. Scale bars, 1 mm.

Supplementary Materials). The design parameters of the microrobots are listed in table S1, and their layouts are shown in Fig. 1C. We proposed the use of scaffold-type microrobots on which cells can be cultured and differentiated in 3D and for which the porosity can be customized depending on the size and characteristics of the target cell. Four types of 3D scaffold microrobots were fabricated by 3D laser lithography using a photocurable polymer with a pore size of 15 μm, which was selected with consideration to the size of the stem cell (Fig. 1D). The microrobots were magnetized and made biocompatible by deposition of nickel and titanium layers.

The magnetic manipulator generates magnetic fields in a 3D workspace with a field intensity B and field gradient ∇B (see the Supplementary Materials). The cylindrical and hexahedral microrobots were manipulated using an external magnetic field gradient (Fig. 1, E and F) (*15*). Application of a rotating magnetic field induced corkscrewing and rolling motions of the helical and spherical microrobots, respectively (Fig. 1, E and F, and movie S1). The external rotating magnetic field caused the helical microrobot to rotate along its long axis, generating a 3D corkscrewing motion with high propulsion efficiency. The helical and spherical microrobots were precisely controlled along a trajectory using the rotating magnetic field (Fig. 1G and movie S1).

The velocities of the microrobots in deionized (DI) water were also evaluated with various rotating frequencies (fig. S1). A single rotation of the helical microrobot will propel it one pitch (80 μm) if there is no slippage, with an ideal corkscrew motion. The spherical microrobot will be propelled 251.2 μm ($2\pi \times$ radius = 251.2 μm) under a single rotation if there is no slippage. Therefore, the spherical microrobot will move 3.14 times further and faster than the helical microrobot in the proposed design. The other different aspect is that the helical microrobot is propelled by a corkscrew motion, so it can swim in a 3D fluidic environment, whereas the spherical microrobot cannot swim in a 3D fluidic environment but can roll up and down in curved hilly channels, such as blood vessels and microfluidic channels. The spherical microrobot can also roll on the surface of a tissue by overcoming the adhesion force. To demonstrate this, we manipulated the helical and spherical microrobots to move through vertical and horizontal microfluidic channels in a confined fluidic environment (fig. S2 and movie S1).

Hippocampal NSC culture and delivery in vitro

Figure 2 shows immunofluorescence and SEM images of hippocampal NSCs after proliferation and differentiation on 2D plates and 3D microrobots. The NSCs on microrobots differentiated into astrocytes, oligodendrocytes, and neurons after 72 hours. The SEM images show that differentiated neurons became attached to, and were entangled with, the microrobot scaffolds. NSC attachment to and differentiation on helical and spherical microrobots was uniform (fig. S3 and movie S2; cell counts are shown in fig. S4). Movie S3 shows magnetic manipulation of the helical and spherical microrobots with attached hippocampal NSCs, demonstrating that the microrobots enabled attachment, proliferation, and differentiation of hippocampal NSCs for stem cell transplantation.

To demonstrate the feasibility of targeted cell delivery using the microrobots in a BoC, we manipulated microrobots loaded with human colorectal carcinoma (HCT116) cells in the BoC mimicking an organ network, which is an in vivo–like in vitro physiological system (Fig. 3). The liver-tumor microorgan network comprised four liver microtissues (MTs) and one tumor MT fluidically interconnected by a microfluidic

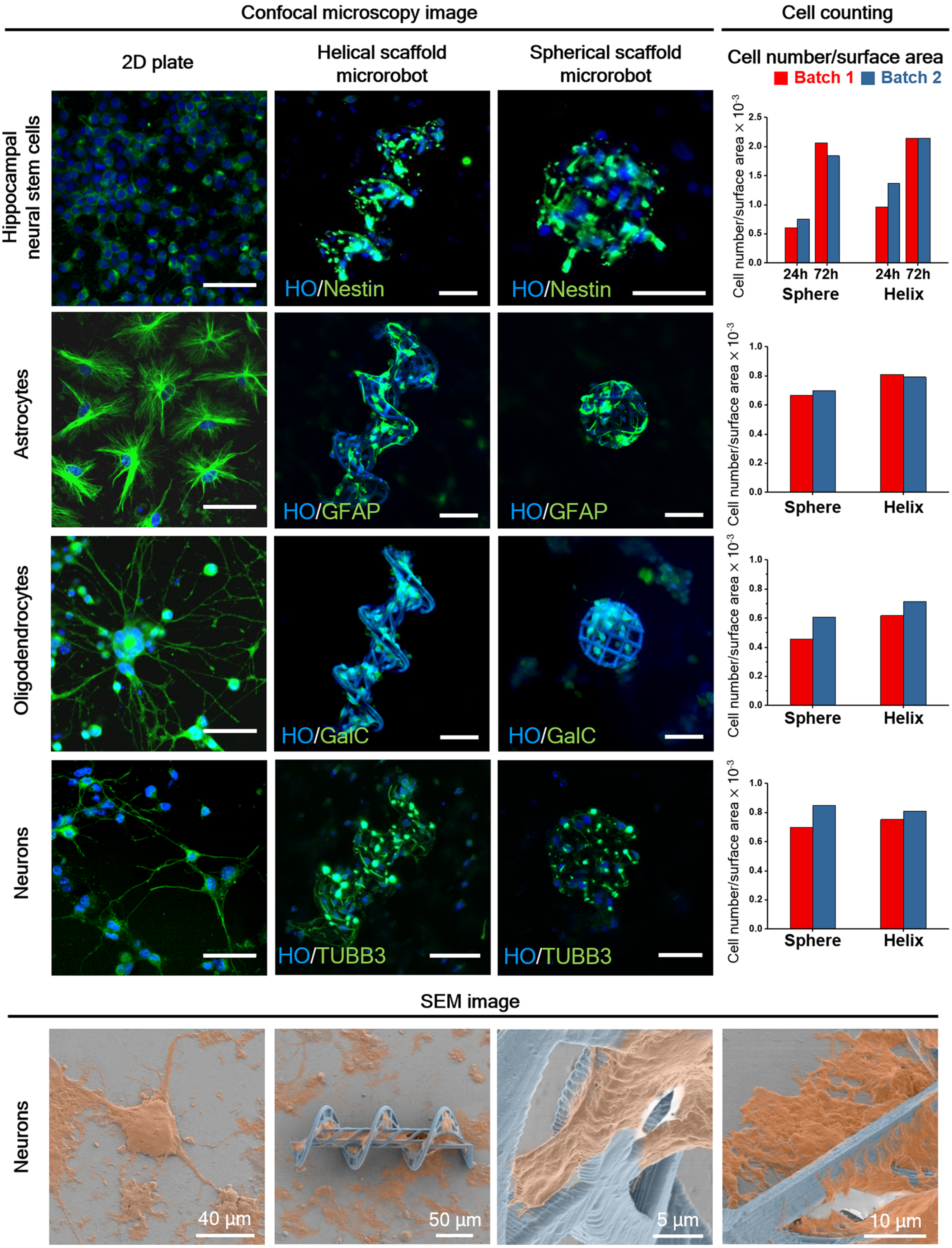

Fig. 2. Immunofluorescence and SEM images of hippocampal NSCs on microrobots. Immunofluorescence images showing the hippocampal NSCs after 72 hours of culture; differentiated astrocytes, oligodendrocytes, and neurons after 72 hours of differentiation; and the numbers of hippocampal NSCs after 24 and 72 hours of culture and of differentiated astrocytes, oligodendrocytes, and neurons after 72 hours of differentiation. SEM images of differentiated neurons on a substrate and on a microrobot with entangled neurites. Staining for markers of different cell types (nestin for NSCs, GFAP for astrocytes, GalC for oligodendrocytes, and Tubb3 for neurons); Hoechst 33342 counterstaining was performed to visualize the nuclei (two types of microrobots were used in each experiment, and each experiment was repeated two times).

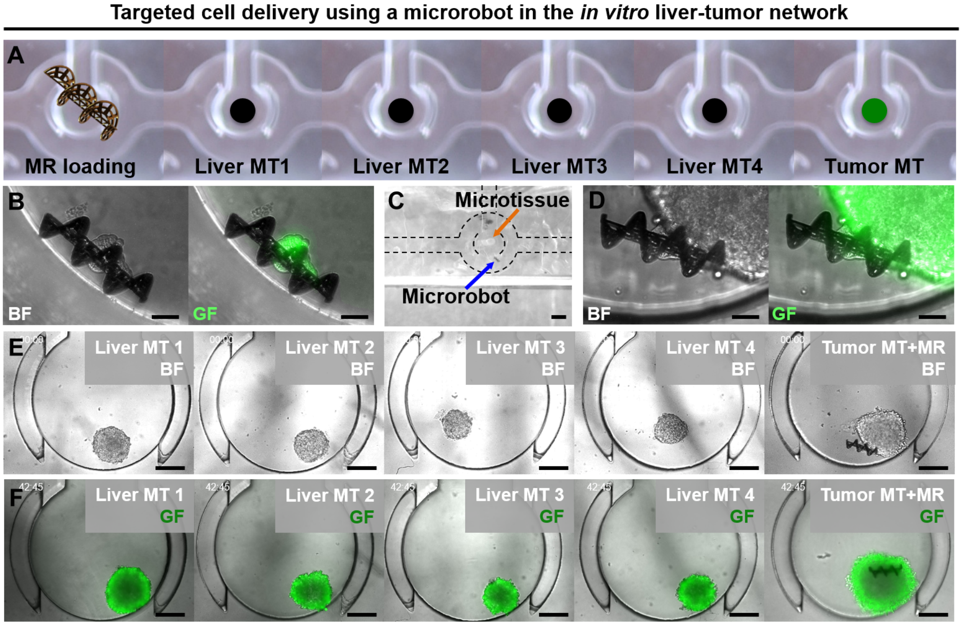

Fig. 3. Targeted cell delivery using a microrobot in a BoC. Targeted HCT116 cell delivery using a microrobot in an in vitro liver-tumor network by bright-field (BF) and Calcein AM–stained green fluorescence (GF) images. (**A**) Configuration of a cell-loaded microrobot, liver, and tumor microorgans in the microfluidic BoC. (**B**) Microrobot with attached HCT116 cells placed in a chamber (scale bars, 50 μm). (**C**) Movement of a microrobot to the target tumor MT, passing four liver MTs (scale bar, 500 μm). (**D**) Arrival of the microrobot at the target tumor MT (scale bars, 50 μm). Liver and tumor MTs with a cell-loaded microrobot before (**E**) and after (**F**) cultivation for 42 hours (scale bars, 200 μm).

channel. A microrobot with attached HCT116 cells was introduced into the BoC and reached the tumor MT after passing the liver MTs under the control of a rotating magnetic field. HCT116 cells on the microrobot adhered to and proliferated within the tumor MT for about 42 hours. Fluorescence imaging of the cells attached on the microrobot was conducted to visualize the live and dead cells with green and red fluorescence, respectively. We then compared the live/dead fluorescence of the cells before and after electromagnetically driven actuation of the cell-attached microrobots in the culturing medium to investigate the viability of the cells after the magnetic manipulation. Because the cells experience external forces such as hydrodynamic shear force and magnetic fields during the locomotion of the microrobot, there may be effects on cell viability. Whereas green fluorescence was observed well, red fluorescence was hardly detected from the cells on the microrobot, either before or after magnetic manipulation [fig. S6A (i and ii)]. This indicates that no notable reduction in cell viability occurred during the locomotion of the microrobots.

We additionally measured adenosine triphosphate (ATP) content in the cells for quantitative analysis of cell viability. No significant decrease was observed from the cells on the microrobot after magnetic manipulation compared with cells that were seeded with the same number of cells and aggregated without the microrobot (fig. S6B). This also indicates that the cells were not notably affected by their exposure to external forces during the locomotion of the microrobot. The HCT116 cells on the microrobot were observed by immunofluorescence staining and confocal laser microscopy. Alexa Fluor 488–conjugated phalloidin was used to label the cytoskeletal area, and 4′,6-diamidino-2-phenylindole dihydrochloride (DAPI) was used to counterstain the nuclei of the HCT116 cells. As shown in fig. S6C, even after magnetic manipulation, phalloidin and DAPI localized to the tumor cell periphery and nuclei with no major changes in the tumor cell morphology. This finding indicates that the electromagnetically driven locomotion of the microrobot most likely did not cause any cytotoxic effects. No reductions in cell or MT viability were detected during loading, transport, or culture (see figs. S5 and S6 and movies S4 and S5 for details).

Ex vivo manipulation of the microrobots

The ex vivo manipulation of the microrobots in a brain blood vessel is shown in Fig. 4. Figure 4 (A and B, respectively) shows a schematic and photograph of the experimental setup for ex vivo microrobot manipulation in the blood vessel of a rat brain. The brain becomes transparent when observed by the CLARITY technique, so that the microrobots can be localized and visualized during manipulation (*40*). Using a Hamilton syringe (33-gauge needle), the microrobots were injected into the internal carotid artery (ICA), which is located before the bifurcation of the anterior cerebral artery (ACA) and middle cerebral artery (MCA). Transparent blood vessels were filled with DI water, and the helical and spherical microrobots were controlled by a rotating magnetic field at 2 Hz with a magnetic field intensity of 15 mT. The helical and spherical microrobots were propelled by corkscrew and rolling motions, respectively, and controlled in the desired directions and positions (Fig. 4, C and D and movie S6). The microrobots were moved from the ICA to the ACA (left blood vessel) and MCA (right blood vessel). Next, to verify their controllability ex vivo in a brain ventricle, we applied the microrobots to a slice of mouse brain in artificial cerebrospinal fluid (CSF). The spherical and helical microrobots reached the ventricle and could be manipulated (Fig. 4E and movie S7), confirming their ability to deliver therapeutic agents to brain ventricles and blood vessels using an appropriate imaging modality. Detailed information on organotypic brain slice culture and transcardial perfusion fixation of the rat brain is provided in the Supplementary Materials.

In vivo stem cell transportation using the microrobots

Human nasal inferior turbinate-derived MSCs (hTMSCs) were cultured on the spherical microrobots (Fig. 5A). It is known that stem cells are not immunogenic when used in allogeneic transplantation. In the previous study in mouse, rat, and rabbit, no immune responses were exhibited in the animal experiments using the same human nasal stem cells without immunosuppressive medicine (*41*–*43*). The proportion of viable cells on day 3 of culture was 92% (Fig. 5B), as determined by the hanging drop cell culture method (fig. S7 and movie S8). In this way, the hTMSCs were immobilized on the microrobots for transplantation in an athymic BALB/c nude mouse (6 to 8 weeks of age, male, 30 g). In this in vivo experiment, fluorescence images and bright-field photographs were obtained using the In Vivo Imaging System (IVIS) Spectrum instrument and were analyzed by Living Image software ver. 4.5 (PerkinElmer, Boston, MA, USA). Microrobots carrying hTMSCs (10^5 cells per 100 microrobots) were

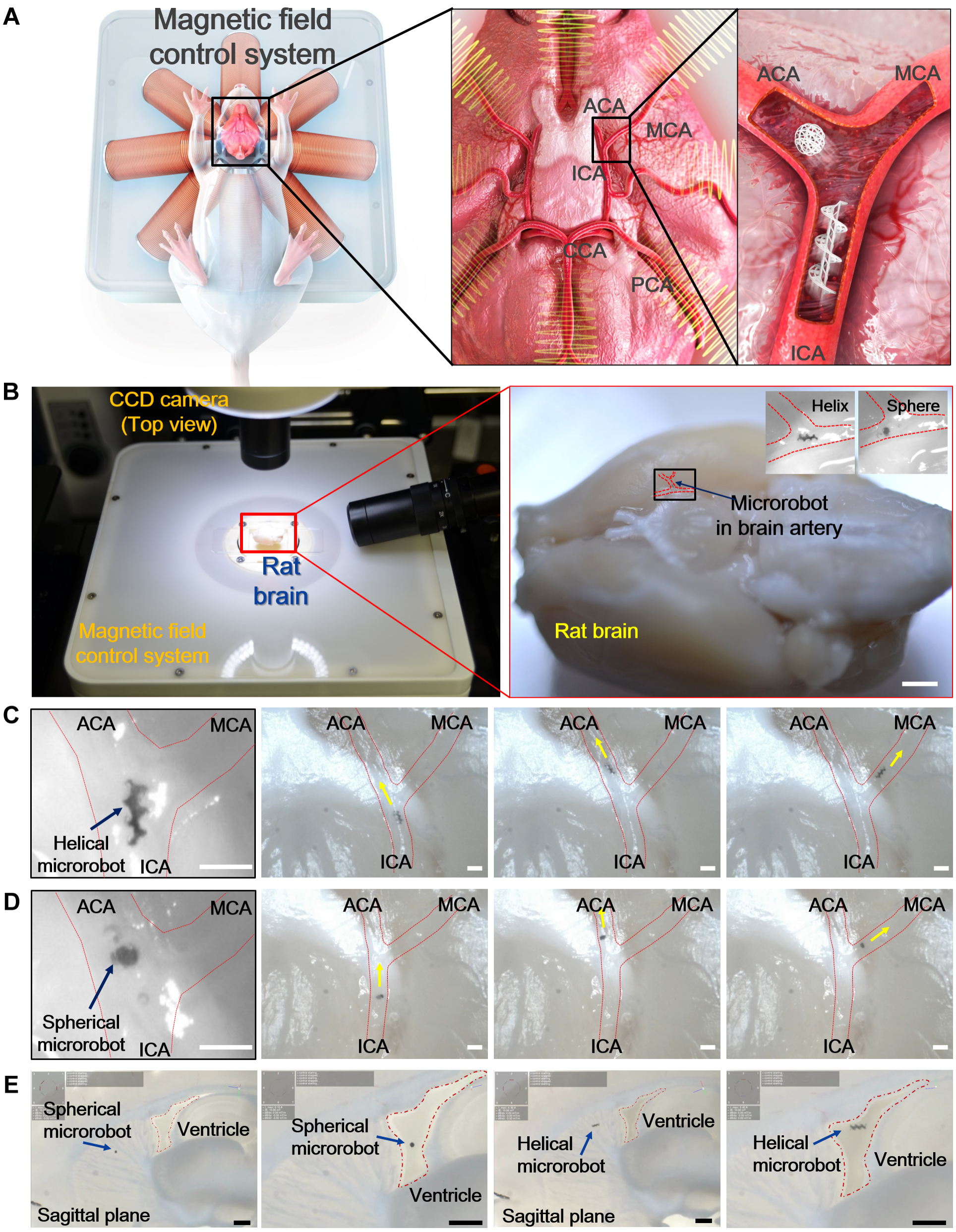

Fig. 4. Magnetic actuation of the microrobots in the brain ex vivo. (**A**) Ex vivo model of a brain blood vessel and the magnetic field control system. (**B**) Experimental setup for magnetic manipulation and a fixed rat brain with transparent blood vessels. Scale bar, 2 mm. (**C** and **D**) Snapshots of helical and spherical microrobots in a transparent brain blood vessel during magnetic manipulation (ICA, ACA, and MCA). Scale bars, 200 μm. (**E**) Positional control of the spherical and helical microrobots from the surface of a brain slice to a ventricle. Scale bars, 500 μm.

dispersed in 5 ml of phosphate-buffered saline (PBS) and injected into the intraperitoneal cavity of an anesthetized nude mouse (Fig. 5C); after injection, no external force was applied to the microrobots. Attachment of cells to the microrobots was confirmed by detection of a fluorescence signal near the injection site. The microrobots were manipulated rightward by a 21 T/m external magnetic field gradient (∇B) for 60 s at 2, 5, and 8 min. After three rightward pulls, the center of the fluorescence signal had moved 1.9 mm in the direction of the applied magnetic field gradient (Fig. 5C). The distance moved was 24-fold the microrobot body length (80 μm) and 125-fold the cell diameter (15 μm). Therefore, cell-loaded microrobots could be manipulated in vivo.

DISCUSSION

We developed magnetically actuated scaffold-type microrobots as a platform for precise stem cell delivery and transplantation in vitro, ex vivo, and in vivo. The microrobots were fabricated by 3D laser lithography and facilitated the attachment, proliferation, and differentiation of hippocampal NSCs, HCT116 cells, and hTMSCs. Propulsion of the microrobots by rolling and corkscrewing motions generated by the rotating magnetic field was more efficient than that generated by a pulling motion and, as such, was more suitable for use in biological fluids. The microrobots were developed and characterized for targeted delivery of stem cells in low Reynolds (Re) number environments that mimicked slow biofluid flow and diffusion-dominated low-viscosity CSF (viscosity, 0.7 mPa·s) (*44*–*48*). Furthermore, the microrobots were manipulated in DI water and PBS (viscosity of about 1 mPa/s). However, it is necessary to study microrobot behavior in various physiological environments. Recently, the behaviors of fully iron magnetic biocompatible 3D microrobots were reported under various fluidic conditions (*49*). The microrobot was tested at various Re numbers by adjusting the viscosity and flow rate of the liquid. It could move in a liquid with a viscosity of 100 mPa/s without flows, which is 100 times lower compared with 1 mPa/s liquid without flow, which was used in this study. It could also swim upstream in up to 63 μm/s of aqueous fluid flow (1 mPa/s). We show here that it will be possible to manipulate fully iron 3D microrobots in various bodily fluids. We will continue to study microrobot-based stem cell delivery under various physiological fluidic conditions.

In general, 3D cell culture is considered superior to 2D cell culture in terms of mimicking the structural and functional complexity of tissue. In this study, after delivery by the microrobots, the cells proliferated and differentiated into astrocytes, oligodendrocytes, and neurons. Because of its larger surface area, the helical microrobot showed higher cell loading capacity than the spherical microrobot. The loading capacity and controllability of the microrobots require improvement before their clinical application.

HCT116 cells were delivered to a target area using the microrobot in a BoC microfluidic channel interconnecting the 3D cultured MTs, which suggests the potential of the microrobots for in vitro cell delivery. HCT116 cells were loaded on the microrobot and delivered from the loading chamber to a target chamber containing a target MT, which

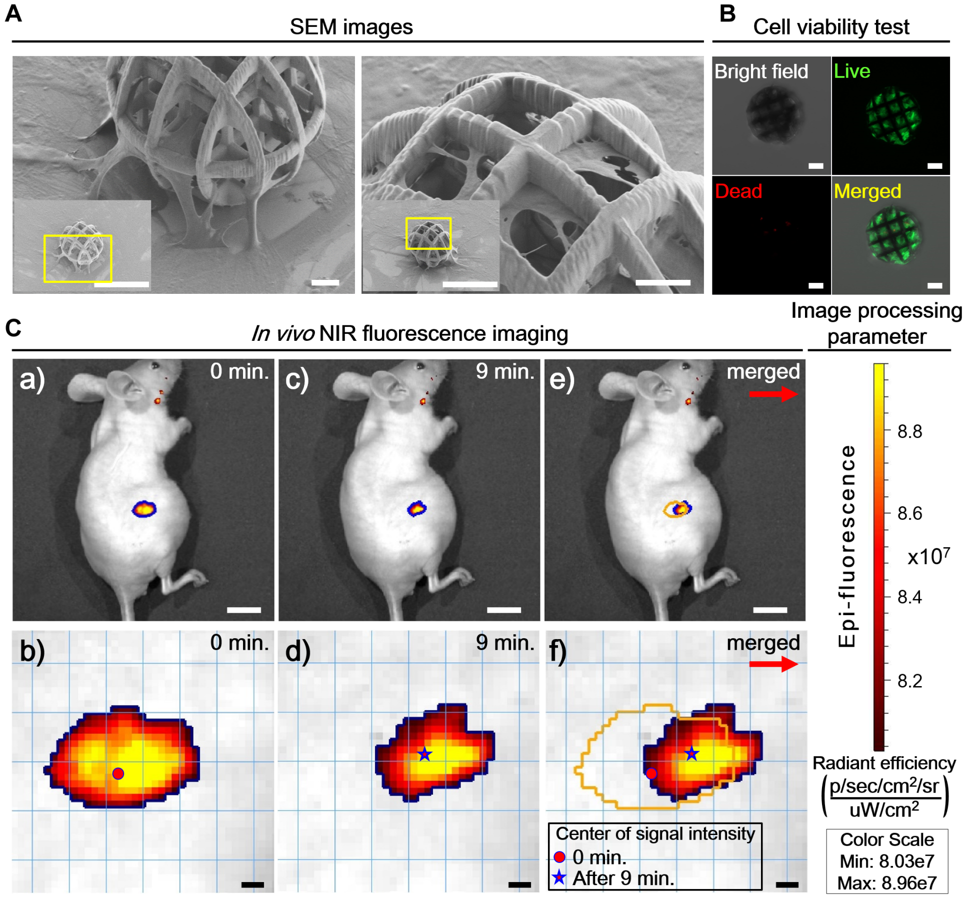

Fig. 5. In vivo MSC transportation using magnetically actuated microrobots. (**A**) SEM images of hTMSCs attached to a spherical microrobot. Scale bars, 10 μm; insets, 100 μm. (**B**) Viability of hTMSCs on a microrobot after 3 days (green, live cells; red, dead cells). Scale bars, 20 μm. (**C**) In vivo transportation of microrobots carrying hTMSCs using an external magnetic field: (a) and (b) after injection, (c) and (d) after magnetic actuation rightward (red arrow), (e) and (f) merged images at 0 and 9 min. The distance moved was 1.9 mm, which is 24-fold the length of a microrobot and 120-fold the diameter of an hTMSC. Scale bars, 10 mm [(a), (c), and (e)] and 1 mm [(b), (d), and (f)].

suggests that this system can be used to study the interactions among MTs (cellular communication) in a BoC for targeted therapeutics using the microrobots. The maneuverability and controllability of the microrobots were demonstrated ex vivo; thus, the microrobots may be used in brain blood vessels and ventricles if they can be localized by an imaging modality (*50*). However, the development of this system is still in its early stages with respect to use in actual in vivo applications, because real-time visualization and localization are required for precise manipulation of the microrobots in in vivo fluidic environments. Last, hTMSCs were cultured on microrobots and manipulated in the intraperitoneal cavity of a nude mouse. The nude mouse was used because it facilitates localization of the microrobots by IVIS. This in vivo experiment showed the feasibility of stem cell and cell cluster delivery using microrobots. The stem cells carried by the microrobot were detected by in vivo near-infrared fluorescence imaging. After being delivered to the target area, hTMSCs could be differentiated into, for example, chondrocytes, osteocytes, and neural cells for therapeutic purpose.

Li *et al.* (*38*) previously evaluated microrobot performance both in vitro and in vivo using magnetic field gradients of 4 to 9 and 20 T/m, respectively. Go *et al.* (*39*) used a 1.8-T/m gradient to manipulate microrobots in the absence of cells. Clinical magnetic resonance imaging (MRI) scanners typically feature a magnetic field of 1.5 to 3 T, and a 7-T system has recently been approved by the U.S. Food and Drug Administration (FDA) for clinical use in the United States (*51*, *52*). Commercial MRI platforms can generate magnetic field gradients ≥24 T/m. Here, we used a magnetic field gradient of 21 T/m and a constant magnetic field of 92 mT for the in vivo cell transportation experiment described in fig. S8; these values are comparable to those of previous studies on microrobot manipulation in vivo and also to those of clinical MRI scanners. It is true that 21 T/m is somewhat high but may be acceptable when seeking to establish proof of concept. We will reduce the field gradient as we improve the animal model and further adapt the magnetic control technology.

To precisely control microrobots in vivo, it is important to actually see them as they move. Unfortunately, our magnetic manipulator was not compatible with the IVIS. Thus, we used a simple manipulation system; a permanent magnet was used to pull hTMSC-loaded microrobots into the intraperitoneal cavity of a nude mouse located within the IVIS. A rotating magnetic field was not available inside the IVIS. Such simple manipulation reduced the available degrees of freedom; the microrobots could not be controlled in a sophisticated manner within the IVIS. This is the principal reason why the distance moved was small and why a high magnetic field gradient was used. All previous studies faced the same issues, because they all used high magnetic field gradients for in vivo microrobot control. This issue may be solved by incorporating a rotational magnetic field into the IVIS or another real-time imaging system. We showed that microrobots could be efficiently controlled in models of various physiological environments by accurately controlling the rotating magnetic field using a magnetic control system (Figs. 3 and 4). We are currently integrating a 3D magnetic manipulator with a real-time imaging system to improve microrobot control in vivo. This will allow us to manipulate microrobots over longer distances using a lower magnetic field.

In conclusion, targeted cell delivery using microrobots was successfully demonstrated in the in vitro microorgan network on the BoC platform, which mimics the in vivo environment better than conventional static 2D cell-based methods. The results provide a logical, rapid system by which it is feasible to perform targeted cell delivery using microrobots in a body.

MATERIALS AND METHODS

Design of the microrobots

The microrobots were designed using a computer-aided design (CAD) tool (SolidWorks, Dassault Systèmes, SolidWorks Corp. Inc., USA).

The design parameters are shown in table S1. The line width, the pore size, and the microrobot size were determined on the basis of stem cell size and cell delivery quantity. Figure 1C shows the CAD designs for the microrobots used in this study.

Fabrication of the microrobots

The glass substrate (2 cm^2) was cleaned, and IP-Dip (a photoresist; Nanoscribe GmbH, Eggenstein-Leopoldshafen, Germany) was applied at the center of the substrate (Fig. 1B). The substrate was adhered to the holder with glue and inserted into the 3D laser lithography system (Photonic Professional GT; Nanoscribe GmbH). The CAD design for each microrobot was loaded onto the machine for laser writing. The writing code contained scanning speed, laser power, and slice distance for each microrobot (*15*). These parameters were optimized for a designated structure by testing the writing. The 780-nm setting of a femtosecond laser was used, and the features were realized by the two-photon absorption method. The laser power and scanning speed used for the 3D laser lithography were 1.8 mW/s and 60 μm/s, respectively. After laser writing, the structures were polymerized and developed with an SU-8 developer for 5 min at room temperature. After fabrication of the structures, 170-nm nickel and 20-nm titanium layers were deposited with a sputtering system (SRN-110; Sorona Inc., Pyeongtaek, South Korea) for magnetization and biocompatibility, respectively. The spherical microrobot has shape magnetic anisotropy due to its radially nonsymmetrical design and the nonuniform metal deposition of the sputtering system. Thus, it has a magnetic easy axis; the magnetic orientation must be aligned with the external magnetic field to generate torque to execute a rolling motion, although its shape appears spherical.

Fabrication of the microfluidic channels

The microfluidic channels were fabricated using MEMS fabrication technology. A 4-inch silicon wafer was used for SU-8 (Microchem Corp., Newton, MA, USA) coating on the wafer with a spin coater at 3000 rpm for 30 s to achieve a thickness of 150 μm. The wafer was then baked on a hotplate for 5 min at 65°C and 30 min at 95°C. Photolithography was performed using an MA8 mask aligner (SÜSS MicroTec AG, Garching, Germany) with an I-line (365 nm) ultraviolet source at 700 mJ/cm^2. The wafer was then developed in an SU-8 developer for 20 min, and 150-μm-thick channel patterns were achieved for use as a mold. Polydimethylsiloxane (PDMS) elastomer (Sylgard 184; Dow Corning, Midland, MI, USA) was poured into the mold, bubbles in the PDMS were removed using a vacuum chamber, and the mold was cured in an oven for 3 hours at 70°C. The cured PDMS was released from the mold and attached onto a glass slide after surface treatment with plasma. The resulting microfluidic channel with a height of 150 μm was used for microrobot manipulation.

Magnetic manipulation

The microrobots were manipulated using a magnetic manipulator (MiniMag; Aeon Scientific AG, Schlieren, Switzerland) with eight electromagnetic coils configured in a hemispherical shape. Figure 4B shows the experimental setup used for magnetic manipulation. Magnetic fields (B) and field gradients (∇B) were generated in a 3D working space to control the microrobots. The microrobots were detached from the substrate using a probe tip and placed in DI water. The cylindrical and hexahedral microrobots were manipulated using a magnetic field gradient (∇B) that transposed them using magnetic pulling. Through direct pulling with a field gradient, we conducted manual and automatic targeted controls. The spherical and helical microrobots were rotated using a rotating magnetic field (B) that generated the propulsion force. The manipulations of the helical and spherical microrobots are shown in movie S1 and Fig. 1G for writing "BMR." The size of each letter was 1.5 mm by 2.5 mm, and the microrobots were controlled manually. Images were acquired from the top-side camera. The helical and spherical microrobots were manipulated in horizontal and vertical microfluidic channels, respectively. Each microrobot was loaded into the robot-loading port of the microfluidic chip after the channel was filled with DI water. The microfluidic channel was placed horizontally and vertically on the workspace of the magnetic manipulator, and the top- and side-view cameras were used to capture the videos (fig. S2 and movie S1). The helical microrobot moved with a corkscrew motion and tracked the channel. The spherical microrobot rolled along the slope to climb a hilly channel. This experiment confirmed that it was possible to manipulate microrobots in confined curvy environments, such as blood vessels. Figure S2 (A and B) was acquired by the top-view camera of a helical microrobot in the horizontal microfluidic channel and by the side-view camera of a spherical microrobot in the vertical microfluidic channel, respectively.

Characterization of the magnetic manipulation

Figure 4B shows an image of the experimental setup for the electromagnetic manipulation system, top-view and side-view cameras for recording, and the light source. The recorded videos were analyzed at 15 frames/s to determine the velocities of the microrobots. The normalized input current values were calculated using Eq. 1 with an acquisition rate of 1000 Hz, where I_1 to I_8 are the target currents for each coil:

$$I_{\text{norm}} = \sqrt{I_1 + I_2 + \ldots + I_8} \tag{1}$$

Hippocampal NSC culture and differentiation

All procedures for the care and use of laboratory animals were approved by the Institutional Animal Care and Use Committee (no. 0014) at the Daegu Gyeongbuk Institute of Science & Technology (DGIST; Daegu, South Korea). NSCs were isolated from the hippocampus of 7-week-old female Sprague-Dawley rats and cultured in chemically defined serum-free media containing Dulbecco's modified Eagle's medium (DMEM)/Ham's F12 (catalog no. 12400-024; Invitrogen, Carlsbad, CA, USA) with basic fibroblast growth factor (bFGF; 20 μg/ml) (catalog no. 100-18B; PeproTech, Rocky Hill, NJ, USA), sodium bicarbonate (1.27 g/liter) (S6014; Sigma-Aldrich, St. Louis, MO, USA), 1% penicillin/streptomycin (SV30010; HyClone Laboratories Inc., Logan, UT, USA), and N2 supplements [insulin (5 mg/liter), putrescin (16 mg/liter), transferrin (100 mg/liter), 30 nM sodium selenite, and 20 nM progesterone; all from Sigma-Aldrich] (*53*, *54*). Stock solutions of each component were prepared separately and later mixed and added to the DMEM/F12 medium.

Hippocampal NSCs were grown on plates coated with poly-L-ornithine (PLO; 10 μg/ml; 3655; Sigma-Aldrich) for 8 hours and then with laminin (5 μg/ml) (354232; BD Biosciences, San Jose, CA, USA) overnight. For differentiation, hippocampal NSCs were grown with microrobots on sterilized glass substrates coated with PLO and laminin at a density of ~1 × 10^5 cells/ml. Hippocampal NSCs were incubated for 24 hours in the culture medium, which was then replaced with the differentiation medium for each lineage. The culture medium was supplemented with (i) 1 μM retinoic acid (RA; BML-GR100-5000; Enzo Life Sciences Inc., Farmingdale, NY, USA) and 5 μM forskolin

(BML-CN100-0100; Enzo) for neurons; (ii) 1 μM RA, bFGF (2 ng/ml), and 1% fetal bovine serum (FBS; SH30071.03HI, HyClone Laboratories Inc.) for oligodendrocytes; and (iii) 1 μM RA and 5% FBS for astrocytes (*3*). Every 2 days, half of the differentiation medium was replaced with fresh differentiation medium. The hippocampal NSCs were very pure before the onset of differentiation. Homogeneous expression of nestin (an NSC marker) by such cells can be seen in Fig. 2. We calculated the proportions of differentiated astrocytes, oligodendrocytes, and neurons obtained in five separate experiments (fig. S3I). Differentiation into each neural lineage was induced separately on different microrobots. Thus, the levels of differentiation into neurons were obtained in experiments that did not evaluate differentiation into astrocytes or oligodendrocytes.

Immunostaining to immunocytochemistry

For immunostaining, the cells on the substrates with microrobots were fixed in 4% paraformaldehyde for 10 min, permeabilized with 0.1% Trton X-100 in antibody dilution buffer (003218; Invitrogen) for 10 min, and incubated overnight with primary antibodies diluted in buffer. The following day, cells were washed twice with PBS (Welgene, Gyeongsan, South Korea), incubated for 1 hour with secondary antibodies, and stained with Hoechst 33342 (H1399; Invitrogen) for 8 min to counterstain the cell nuclei. After three washes with PBS, the substrates were mounted on cover glasses in mounting solution (S3023; Dako, Santa Clara, CA, USA). The primary antibodies targeted nestin (catalog no. 27952; Abcam, Cambridge, UK), tubulin β-III (Tubb3; catalog no. MAB1637; Millipore, Darmstadt, Germany), galactocerebroside (GalC; catalog no. AB142; Millipore), and glial fibrillary acidic protein (GFAP; catalog no. RA22101; Neuromics Inc., Minneapolis, MN, USA). The secondary antibodies were anti-mouse (A11001; Invitrogen) or anti-rabbit (A11034; Invitrogen) conjugated with Alexa Fluor 488. The images were taken with a confocal microscope (Zeiss LSM 780; Carl Zeiss, Oberkochen, Germany) using a 63×/1.0 oil objective equipped with a multi-argon laser [Alexa Fluor 488, excitation (Ex.) at 488 nm and emission (Em.) at 525 nm; and Hoechst 33342, Ex. 405 nm and Em. 458 nm]. For SEM images, the substrates with microrobots were fixed in 4% paraformaldehyde for 10 min at room temperature after washing with sterilized DI water. The 3D distribution of the cells on the helical and spherical microrobots is shown in fig. S3. The images were reconstructed from fluorescence z-stack images. Three-dimensional graphics of the differentiation process are shown in movie S2.

Cell counting

The number of cells on each microrobot was counted using ImageJ software (fig. S4, A to D). NSCs grown on helical and spherical microrobots were counted after 24 and 72 hours of culture (fig. S4A) and again after differentiation (fig. S4, B to D). We normalized the number of cells on microrobots by dividing the cell number by the microrobot surface area (Fig. 2). We used both helical and spherical microrobots for cell culture; two independent differentiation experiments were performed, each of which featured one helical and one spherical microrobot. Variabilities between the numbers of cells present within the same surface area were recorded. After proliferation for 24 hours, twice as many cells were present on the helical microrobots compared with the number of cells on the spherical microrobots. These data suggest that more cells attached to the helical microrobot than to the spherical type due to the larger surface area. However, each microrobot had different characteristics that may have uses for different applications.

Magnetic manipulation of the microrobots with hippocampal NSCs

The helical and spherical microrobots were manipulated using the magnetic manipulator after culturing with cells. The hippocampal NSCs were cultured on the surface of the microrobots following the same protocol as on a cell culture plate. Movie S3 shows the manipulation results for cell-cultured microrobots in the PBS solution. The movement of the helical microrobots changed from a corkscrew motion without cells to a tumbling motion with a decreased velocity with cells. The movement of the spherical microrobots was almost the same after cell culture as it was before cell culture.

Targeted HCT116 cell delivery using a microrobot in a BoC

First, the BoC microfluidic platform was fabricated using a conventional soft lithography process. An SU-8 master mold was made on a 6-inch silicon wafer using standard photolithography techniques. The master mold contained relief patterns for microfluidic channels for media perfusion and chambers for MT culturing. Then, PDMS was prepared by mixing the base with its curing agent (10:1). The mixture was poured on the SU-8 master mold, cured at 65°C for 4 hours, and peeled from the master mold. The PDMS channels were bonded with 1-mm-thick PDMS substrate to form enclosed microfluidic channels.

Second, liver MT and tumor MT were prepared using human hepatoma (HepG2) and HCT116 cells, respectively. Cultures of both cells were purchased from the Korean Cell Line Bank in South Korea. For both HepG2 and HCT116, 300 cells were seeded with 100 μl of media in a U-bottom 96-well plate (Thermo Fisher Scientific, Waltham, MA, USA). The cell culture medium, RPMI 1640 (Thermo Fisher Scientific), was mixed with 10% FBS, penicillin (100 g/ml), and streptomycin (10 g/ml). After incubation for 4 days at 37°C, 5% CO_2, and >80% humidity, the cells aggregated by themselves in the wells, forming spherical MTs of HepG2 and HCT116 cells with diameters of about 200 and 250 μm, respectively. Four HepG2 MTs and one HCT116 MT were placed into the BoC platform as representative liver and tumor microorgan models, respectively. They were physically separated by microchambers, but fluidically interconnected via a microfluidic channel, creating the in vitro liver-tumor network.

Third, an HCT116 cell suspension was prepared with a concentration of 50 cells/ml, and 200 μl of the suspension (containing about 10 cells) was added with a single microrobot to each well of a U-bottom micro 96-well plate. All of the cells gathered in the center of the U-bottom and then attached to the microrobot owing to gravity and the antiadhesion coating on the surface of the U-bottom substrate. After culturing in a cell culture incubator for 3 days, HCT116 cells successfully adhered onto the microrobot, as shown in fig. S5A. Cell viability was assessed by green fluorescent imaging induced by Calcein AM fluorescent dye. Live cell staining was observed, which indicated that the cells were viable even after being loaded onto the microrobot. The cells were stained with the LIVE/DEAD Cell Imaging Kit (product no. R37601, Thermo Fisher Scientific, USA), which distinguishes live cells according to the presence of ubiquitous intracellular esterase activity, as determined by the enzymatic conversion of the nearly nonfluorescent cell-permeant Calcein AM to the intensely fluorescent calcein, which is well retained within live cells. The red dye only enters cells with damaged membranes and then fluoresces brightly on binding to DNA. Green fluorescence was measured using Ex./Em. 488-nm/515-nm filters, and red fluorescence was measured with Ex./Em. 570-nm/602-nm filters. One milliliter of the kit solution (a mixture of the green and red fluorescent dyes) was added with an equal volume of cell culture medium into wells containing the HCT116 cells loaded on the microrobot, and then the cultures were incubated for 15 min at room temperature. The stained HCT116 cells were imaged using an inverted microscope (Observer Z1; Carl Zeiss, Oberkochen, Germany) with a 40× objective lens with bright-field, green fluorescence, and red fluorescence filters.

Fourth, the HCT116 cell-loaded microrobot was manipulated using an external rotating magnetic field generated from the magnetic manipulator. The microrobot swam with a corkscrew motion in the microfluidic channel, passing by nontargeted microorgans (liver MTs), and successfully reached the targeted tumor MT (see fig. S5B and movie S4). Upon reaching the tumor MT, the HCT116 cells were still firmly adhered onto the microrobot and exhibited green fluorescence, indicating that no notable reduction in cell viability occurred during the transportation of the cells to the targeted tumor MT.

Next, the microrobot and MTs were cultured in the BoC under media perfusion (1 μl/min) for about 42 hours. As depicted in movie S5, the HCT116 cells on the microrobot aggregated onto the targeted tumor MT and grew without a notable decrease in viability. The liver MTs also appeared to maintain viability. The MTs and microrobot were monitored using time-lapse imaging with 15-min intervals using the same inverted microscope in bright-field mode (movie S5).

In fig. S6A, the cell viability assay was carried out to show how the cells attached to the microrobot were affected during manipulation and delivery. We seeded the cells (10 cells/200 μl) with the microrobot onto the U-bottom microwell, cultured the HCT116 cells to attach onto the microrobot for 3 days, and then stained the cells with the LIVE/DEAD Cell Imaging Kit (product no. R37601, Thermo Fisher Scientific, USA). The live/dead cell viability assay was conducted according to the manufacturer's instructions. Green fluorescence was measured with Ex./Em. 488-nm/515-nm filters, and red fluorescence was measured with Ex./Em. 570-nm/602-nm filters. The microrobots with attached cells were driven by a rotating magnetic field at 10 mT and 10 Hz for 5 min. Red autofluorescence was observed, caused by nonspecific staining of the red fluorescent dye on the exposed microrobot polymer that was not successfully covered by the outermost Ti layer, as depicted in fig. S6A (iii). Because the sputtered Ni and Ti thin film were deposited in 2D, normally from the metal source on the top onto the sample, the entire surface of the 3D microrobot structures could not be perfectly coated, resulting in a few uncovered regions, such as the contact area between the 3D microrobots and the substrate. Therefore, the red fluorescence in the live/dead assay is not fluorescence emitted from dead cells, but the autofluorescence of the microrobot.

The ATP assay was performed to confirm more clearly whether the manipulation of the microrobot affects the attached cells on the microrobot, as shown in fig. S6B. The assay was performed using the CellTiter-Glo 3D kit (Promega, Madison, WI, USA) according to the manufacturer's protocol. The method of coculturing the microrobot and the cells was the same as described above, and only cells (without a microrobot) were seeded on the U-bottom micro 96-well plate in the control group. After incubating for 3 days to allow for cell aggregation on the microrobot, the microrobot was manipulated by a rotating magnetic field at 10 mT and 10 Hz for 5 min, and then the ATP assay was conducted.

Cells were fixed with 4% paraformaldehyde for 30 min at room temperature and then washed twice with PBS. Permeabilization was done for 30 min with 1% Triton X-100 in PBS. Blocking of the antibodies' nonspecific binding was done by incubating the cells for 30 min at room temperature in 3% bovine serum albumin (BSA; Sigma-Aldrich, St. Louis, MO, USA) in PBS. After 1 hour incubation with Alexa Fluor 488 phalloidin (Molecular Probes/Invitrogen) at a 1:40 dilution in 1% BSA in PBS (25 μl/ml), the wells were washed three times using PBS. Then, cells were incubated for 5 min in DAPI (1 μg/ml) in PBS for nuclei counterstaining and washed three times using PBS.

All statistical analysis was conducted by GraphPad Prism computer software (GraphPad Software Inc., San Diego, CA, USA). Two-tailed unpaired *t* test was used to determine statistical significance. *P* values higher than 0.05 were considered as not statistically significant. In this experiment result, the *P* value was 0.7910. Error bars in fig. S6B indicate standard deviation from five samples.

SUPPLEMENTARY MATERIALS

robotics.sciencemag.org/cgi/content/full/4/30/eaav4317/DC1

Fig. S1. The velocities of microrobots under external magnetic fields with various rotating frequencies.

Fig. S2. Manipulation of the helical microrobot in a horizontal microfluidic channel and the spherical microrobot in a vertical microfluidic channel.

Fig. S3. Three-dimensional images of hippocampal NSCs distributed on helical and spherical microrobots.

Fig. S4. The number of proliferated stem cells on the microrobots and the numbers of cells on the microrobots after differentiation into astrocytes, oligodendrocytes, and neurons.

Fig. S5. Targeted HCT116 cell delivery and transplantation using a microrobot in BoC.

Fig. S6. Fluorescence imaging of the cells attached to the microrobot, ATP content in the cells for quantitative analysis of the cell viability of the treatment group, and reconstructed confocal image of the immunofluorescence staining of the HCT116 cells attached to the helical microrobot.

Fig. S7. The process of hanging drop cell culture with a spherical microrobot.

Fig. S8. Measured magnetic field intensity and gradient used for the in vivo experiment.

Table S1. Design parameters for each microrobot.

Movie S1. Magnetic manipulation of the helical and spherical microrobots using a rotating magnetic field.

Movie S2. Three-dimensional animation of the confocal microscopic images of the differentiation of astrocytes, oligodendrocytes, and neurons on the helical and spherical microrobots.

Movie S3. Magnetic manipulation of the helical and spherical microrobots after hippocampal NSC attachment.

Movie S4. Targeted cell delivery in in vitro microorgan network using a magnetically actuated microrobot.

Movie S5. Microtissue cultivation after targeted cell delivery using a microrobot in the BoC.

Movie S6. Manipulation of the helical and spherical microrobots in a rat brain blood vessel for an ex vivo test.

Movie S7. Manipulation of the helical and spherical microrobots in a ventricle of a sagittal brain slice to mimic an in vivo environment.

Movie S8. Magnetic manipulation of the spherical microrobot with attached hTMSCs.

References (*55*–*74*)

REFERENCES AND NOTES

1. F. H. Gage, Mammalian neural stem cells. *Science* **287**, 1433–1438 (2000).
2. O. Lindvall, Z. Kokaia, A. Martinez-Serrano, Stem cell therapy for human neurodegenerative disorders—How to make it work. *Nat. Med.* **10**, S42–S50 (2004).
3. Y.-W. Liu, B. Chen, X. Yang, J. A. Fugate, F. A. Kalucki, A. Futakuchi-Tsuchida, L. Couture, K. W. Vogel, C. A. Astley, A. Baldessari, J. Ogle, C. W. Don, Z. L. Steinberg, S. P. Seslar, S. A. Tuck, H. Tsuchida, A. V. Naumova, S. K. Dupras, M. S. Lyu, J. Lee, D. W. Hailey, H. Reinecke, L. Pabon, B. H. Fryer, W. R. MacLellan, R. S. Thies, C. E. Murry, Human embryonic stem cell–derived cardiomyocytes restore function in infarcted hearts of non-human primates. *Nat. Biotechnol.* **36**, 597–605 (2018).
4. Y. Shi, H. Inoue, J. C. Wu, S. Yamanaka, Induced pluripotent stem cell technology: A decade of progress. *Nat. Rev. Drug Discov.* **16**, 115–130 (2017).
5. C. R. Nitkin, T. L. Bonfield, Concise review: Mesenchymal stem cell therapy for pediatric disease: Perspectives on success and potential improvements. *Stem Cells Transl. Med.* **6**, 539–565 (2017).
6. Y. Shiba, S. Fernandes, W.-Z. Zhu, D. Filice, V. Muskheli, J. Kim, N. J. Palpant, J. Gantz, K. W. Moyes, H. Reinecke, B. Van Biber, T. Dardas, J. L. Mignone, A. Izawa, R. Hanna, M. Viswanathan, J. D. Gold, M. I. Kotlikoff, N. Sarvazyan, M. W. Kay, C. E. Murry,

M. A. Laflamme, Human ES-cell-derived cardiomyocytes electrically couple and suppress arrhythmias in injured hearts. *Nature* **489**, 322–325 (2012).

7. R. A. Barker, M. Parmar, L. Studer, J. Takahashi, Human trials of stem cell-derived dopamine neurons for Parkinson's disease: Dawn of a new era. *Cell Stem Cell* **21**, 569–573 (2017).
8. B. J. Nelson, I. K. Kaliakatsos, J. J. Abbott, Microrobots for minimally invasive medicine. *Ann. Rev. Biomed. Eng.* **12**, 55–85 (2010).
9. M. Sitti, Miniature devices: Voyage of the microrobots. *Nature* **458**, 1121–1122 (2009).
10. S. Fusco, F. Ullrich, J. Pokki, G. Chatzipirpiridis, B. Özkale, K. M. Sivaraman, O. Ergeneman, S. Pané, B. J. Nelson, Microrobots: A new era in ocular drug delivery. *Expert Opin. Drug Deliv.* **11**, 1815–1826 (2014).
11. S. Park, K. Cha, J. Park, Development of biomedical microrobot for intravascular therapy. *Int. J. Adv. Robot. Syst.* **7**, 10.5772/7260 (2010).
12. A. Forgione, *In vivo* microrobots for natural orifice transluminal surgery. Current status and future perspectives. *Surg. Oncol.* **18**, 121–129 (2009).
13. O. Felfoul, M. Mohammadi, S. Taherkhani, D. de Lanauze, Y. Zhong Xu, D. Loghin, S. Essa, S. Jancik, D. Houle, M. Lafleur, L. Gaboury, M. Tabrizian, N. Kaou, M. Atkin, T. Vuong, G. Batist, N. Beauchemin, D. Radzioch, S. Martel, Magneto-aerotactic bacteria deliver drug-containing nanoliposomes to tumour hypoxic regions. *Nat. Nanotechnol.* **11**, 941–947 (2016).
14. F. Ullrich, C. Bergeles, J. Pokki, O. Ergeneman, S. Erni, G. Chatzipirpiridis, S. Pané, C. Framme, B. J. Nelson, Mobility experiments with microrobots for minimally invasive intraocular surgery. *Invest. Ophthalmol. Vis. Sci.* **54**, 2853–2863 (2013).
15. S. Kim, F. Qiu, S. Kim, A. Ghanbari, C. Moon, L. Zhang, B. J. Nelson, H. Choi, Fabrication and characterization of magnetic microrobots for three-dimensional cell culture and targeted transportation. *Adv. Mater.* **25**, 5863–5868 (2013).
16. J. J. Abbott, Z. Nagy, F. Beyeler, B. J. Nelson, Robotics in the small, part I: Microbotics. *IEEE Robot. Autom. Mag.* **14**, 92–103 (2007).
17. J. J. Abbott, K. E. Peyer, M. C. Lagomarsino, L. Zhang, L. Dong, I. K. Kaliakatsos, B. J. Nelson, How should microrobots swim? *Int. J. Robot. Res.* **28**, 1434–1447 (2009).
18. S. Palagi, A. G. Mark, S. Y. Reigh, K. Melde, T. Qiu, H. Zeng, C. Parmeggiani, D. Martella, A. Sanchez-Castillo, N. Kapernaum, F. Giesselmann, D. S. Wiersma, E. Lauga, P. Fischer, Structured light enables biomimetic swimming and versatile locomotion of photoresponsive soft microrobots. *Nat. Mater.* **15**, 647–653 (2016).
19. J. J. Abbott, O. Ergeneman, M. P. Kummer, A. M. Hirt, B. J. Nelson, Modeling magnetic torque and force for controlled manipulation of soft-magnetic bodies. *IEEE Trans. Robot.* **23**, 1247–1252 (2007).
20. H.-W. Tung, M. Maffioli, D. R. Frutiger, K. M. Sivaraman, S. Pané, B. J. Nelson, Polymer-based wireless resonant magnetic microrobots. *IEEE Trans. Robot.* **30**, 26–32 (2014).
21. G.-L. Jiang, Y.-H. Guu, C.-N. Lu, P.-K. Li, H.-M. Shen, L.-S. Lee, J. A. Yeh, M. T.-K. Hou, Development of rolling magnetic microrobots. *J. Micromech. Microeng.* **20**, 085042 (2010).
22. K. E. Peyer, L. Zhang, B. J. Nelson, Bio-inspired magnetic swimming microrobots for biomedical applications. *Nanoscale* **5**, 1259–1272 (2013).
23. K. E. Peyer, S. Tottori, F. Qiu, L. Zhang, B. J. Nelson, Magnetic helical micromachines. *Chem. A Eur. J.* **19**, 28–38 (2013).
24. S. Tottori, L. Zhang, F. Qiu, K. K. Krawczyk, A. Franco-Obregón, B. J. Nelson, Magnetic helical micromachines: Fabrication, controlled swimming, and cargo transport. *Adv. Mater.* **24**, 811–816 (2012).
25. A. Servant, F. Qiu, M. Mazza, K. Kostarelos, B. J. Nelson, Controlled *in vivo* swimming of a swarm of bacteria-like microrobotic flagella. *Adv. Mater.* **27**, 2981–2988 (2015).
26. F. Qiu, L. Zhang, K. E. Peyer, M. Casarosa, A. Franco-Obregón, H. Choi, B. J. Nelson, Noncytotoxic artificial bacterial flagella fabricated from biocompatible ORMOCOMP and iron coating. *J. Mater. Chem. B* **2**, 357–362 (2014).
27. W. Gao, X. Feng, A. Pei, C. R. Kane, R. Tam, C. Hennessy, J. Wang, Bioinspired helical microswimmers based on vascular plants. *Nano Lett.* **14**, 305–310 (2013).
28. D. Walker, B. T. Käsdorf, H.-H. Jeong, O. Lieleg, P. Fischer, Enzymatically active biomimetic micropropellers for the penetration of mucin gels. *Sci. Adv.* **1**, e1500501 (2015).
29. R. Dreyfus, J. Baudry, M. L. Roper, M. Fermigier, H. A. Stone, J. Bibette, Microscopic artificial swimmers. *Nature* **437**, 862–865 (2005).
30. I. S. M. Khalil, H. C. Dijkslag, L. Abelmann, S. Misra, MagnetoSperm: A microrobot that navigates using weak magnetic fields. *Appl. Phys. Lett.* **104**, 223701 (2014).
31. B. Jang, E. Gutman, N. Stucki, B. F. Seitz, P. D. Wendel-García, T. Newton, J. Pokki, O. Ergeneman, S. Pané, Y. Or, B. J. Nelson, Undulatory locomotion of magnetic multilink nanoswimmers. *Nano Lett.* **15**, 4829–4833 (2015).
32. S. Kim, S. Lee, J. Lee, B. J. Nelson, L. Zhang, H. Choi, Fabrication and manipulation of ciliary microrobots with non-reciprocal magnetic actuation. *Sci. Rep.* **6**, 30713 (2016).
33. S.-J. Park, M. Gazzola, K. S. Park, S. Park, V. Di Santo, E. L. Blevins, J. U. Lind, P. H. Campbell, S. Dauth, A. K. Capulli, F. S. Pasqualini, S. Ahn, A. Cho, H. Yuan, B. M. Maoz, R. Vijaykumar, J.-W. Choi, K. Deisseroth, G. V. Lauder, L. Mahadevan, K. K. Parker, Phototactic guidance of a tissue-engineered soft-robotic ray. *Science* **353**, 158–162 (2016).
34. E. M. Purcell, Life at low Reynolds number. *Am. J. Phys.* **45**, 3–11 (1977).
35. Y. Alapan, O. Yasa, O. Schauer, J. Giltinan, A. F. Tabak, V. Sourjik, M. Sitti, Soft erythrocyte-based bacterial microswimmers for cargo delivery. *Sci. Robot.* **3**, eaar4423 (2018).
36. Y. Sun, B. J. Nelson, Biological cell injection using an autonomous microrobotic system. *Int. J. Robot. Res.* **21**, 861–868 (2002).
37. S. Lee, S. Kim, S. Kim, J.-Y. Kim, C. Moon, B. J. Nelson, H. Choi, A capsule-type microrobot with pick-and-drop motion for targeted drug and cell delivery. *Adv. Healthc. Mater.* **7**, 1700985 (2018).
38. J. Li, X. Li, T. Luo, R. Wang, C. Liu, S. Chen, D. Li, J. Yue, S.-h. Cheng, D. Sun, Development of a magnetic microrobot for carrying and delivering targeted cells. *Sci. Robot.* **3**, eaat8829 (2018).
39. G. Go, J. Han, J. Zhen, S. Zheng, A. Yoo, M.-J. Jeon, J.-O. Park, S. Park, A magnetically actuated microscaffold containing mesenchymal stem cells for articular cartilage repair. *Adv. Healthc. Mater.* **6**, 1601378 (2017).
40. E. Lee, J. Choi, Y. Jo, J. Y. Kim, Y. J. Jang, H. M. Lee, S. Y. Kim, H.-J. Lee, K. Cho, N. Jung, E. M. Hur, S. J. Jeong, C. Moon, Y. Choe, I. J. Rhyu, H. Kim, W. Sun, ACT-PRESTO: Rapid and consistent tissue clearing and labeling method for 3-dimensional (3D) imaging. *Sci. Rep.* **6**, 18631 (2016).
41. J. H. Park, J. Y. Park, I.-C. Nam, S.-H. Hwang, C.-S. Kim, J. W. Jung, J. Jang, H. Lee, Y. Choi, S. H. Park, S. W. Kim, D.-W. Cho, Human turbinate mesenchymal stromal cell sheets with bellows graft for rapid tracheal epithelial regeneration. *Acta Biomater.* **25**, 56–64 (2015).
42. H. Lim, S. H. Park, S. W. Kim, K.-O. Cho, Therapeutic potential of human turbinate-derived mesenchymal stem cells in experimental acute ischemic stroke. *Int. Neurol. J.* **22**, S131–S138 (2018).
43. F. Gao, S. M. Chiu, D. A. L. Motan, Z. Zhang, L. Chen, H.-L. Ji, H.-F. Tse, Q.-L. Fu, Q. Lian, Mesenchymal stem cells and immunomodulation: Current status and future prospects. *Cell Death Dis.* **7**, e2062 (2016).
44. H. N. Schwerdt, U. Amjad, J. Appel, A. M. Elhadi, T. Lei, M. C. Preul, R. E. Bristol, J. Chae, In vitro hydrodynamic, transient, and overtime performance of a miniaturized valve for hydrocephalus. *Ann. Biomed. Eng.* **43**, 603–615 (2015).
45. G. D. O. Lowe, A. J. Lee, A. Rumley, J. F. Price, F. G. R. Fowkes, Blood viscosity and risk of cardiovascular events: The Edinburgh Artery Study. *Br. J. Haematol.* **96**, 168–173 (1997).
46. G. Elert, *The Physics Hypertextbook*. Online at https://physics.info/viscosity/.
47. R. S. Rosenson, A. McCormick, E. F. Uretz, Distribution of blood viscosity values and biochemical correlates in healthy adults. *Clin. Chem.* **42**, 1189–1195 (1996).
48. E. Yeom, Y. J. Kang, S.-J. Lee, Changes in velocity profile according to blood viscosity in a microchannel. *Biomicrofluidics* **8**, 034110 (2014).
49. C. C. J. Alcântara, S. Kim, S. Lee, B. Jang, P. Thakolkaran, J.-. Y. Kim, H. Choi, B. J. Nelson, S. Pané, 3D Fabrication of fully iron magnetic microrobots. *Small* **15**, 1805006 (2019).
50. M. Medina-Sánchez, O. G. Schmidt, Medical microbots need better imaging and control. *Nature* **545**, 406–408 (2017).
51. T. Huelnhagen, F. Hezel, T. S. Duarte, A. Pohlmann, C. Oezerdem, B. Flemming, E. Seeliger, M. Prothmann, J. Schulz-Menger, T. Niendorf, Myocardial effective transverse relaxation time T_2^* correlates with left ventricular wall thickness: A 7.0 T MRI study. *Magn. Reson. Med.* **77**, 2381–2389 (2017).
52. O. A. Ilahi, R. S. Staewen, E. F. Stautberg III, A. A. Qadeer, Estimating lengths of semitendinosus and gracilis tendons by magnetic resonance imaging. *Arthroscopy* **34**, 2457–2462 (2018).
53. F. H. Gage, J. Ray, L. J. Fisher, Isolation, characterization, and use of stem cells from the CNS. *Annu. Rev. Neurosci.* **18**, 159–192 (1995).
54. T. D. Palmer, E. A. Markakis, A. R. Willhoite, F. Safar, F. H. Gage, Fibroblast growth factor-2 activates a latent neurogenic program in neural stem cells from diverse regions of the adult CNS. *J. Neurosci.* **19**, 8487–8497 (1999).
55. L. Stoppini, P.-A. Buchs, D. Muller, A simple method for organotypic cultures of nervous tissue. *J. Neurosci. Methods* **37**, 173–182 (1991).
56. A. I. Caplan, Mesenchymal stem cells. *J. Orthop. Res.* **9**, 641–650 (1991).
57. S. Wakitani, T. Saito, A. I. Caplan, Myogenic cells derived from rat bone marrow mesenchymal stem cells exposed to 5-azacytidine. *Muscle Nerve* **18**, 1417–1426 (1995).
58. T. L. Young, S. M. Ronan, A. B. Alvear, S. C. Wildenberg, W. S. Oetting, L. D. Atwood, D. J. Wilkin, R. A. King, A second locus for familial high myopia maps to chromosome 12q. *Am. J. Hum. Genet.* **63**, 1419–1424 (1998).
59. M. F. Pittenger, A. M. Mackay, S. C. Beck, R. K. Jaiswal, R. Douglas, J. D. Mosca, M. A. Moorman, D. W. Simonetti, S. Craig, D. R. Marshak, Multilineage potential of adult human mesenchymal stem cells. *Science* **284**, 143–147 (1999).
60. C. Rosada, J. Justesen, D. Melsvik, P. Ebbesen, M. Kassem, The human umbilical cord blood: A potential source for osteoblast progenitor cells. *Calcif. Tissue Int.* **72**, 135–142 (2003).
61. M. Fradis, J. Danino, L. Gaitini, M. Gershinski, S. Malatskey, A. Golz, M. Goldsher, W. Armush, Inferior turbinectomy versus submucosal diathermy for inferior turbinate hypertrophy. *Ann. Otol. Rhinol. Laryngol.* **109**, 1040–1045 (2000).
62. M. Dominici, K. Le Blanc, I. Mueller, I. Slaper-Cortenbach, F. C. Marini, D. S. Krause, R. J. Deans, A. Keating, D. J. Prockop, E. M. Horwitz, Minimal criteria for defining

multipotent mesenchymal stromal cells. The International Society for Cellular Therapy position statement. *Cytotherapy* **8**, 315–317 (2006).
63. J. Müller, C. Ossig, J. F. W. Greiner, S. Hauser, M. Fauser, D. Widera, C. Kaltschmidt, A. Storch, B. Kaltschmidt, Intrastriatal transplantation of adult human neural crest-derived stem cells improves functional outcome in parkinsonian rats. *Stem Cells Transl. Med.* **4**, 31–43 (2015).
64. Z. Zhang, Q. He, W. Deng, Q. Chen, X. Hu, A. Gong, X. Cao, J. Yu, X. Xu, Nasal ectomesenchymal stem cells: Multi-lineage differentiation and transformation effects on fibrin gels. *Biomaterials* **49**, 57–67 (2015).
65. A. Srinivasan, S.-Y. Chang, S. Zhang, W. S. Toh, Y.-C. Toh, Substrate stiffness modulates the multipotency of human neural crest derived ectomesenchymal stem cells via CD44 mediated PDGFR signaling. *Biomaterials* **167**, 153–167 (2018).
66. J. Zhang, X. Gao, H. Zou, J. Liu, Z. Zhang, Rat nasal respiratory mucosa-derived ectomesenchymal stem cells differentiate into Schwann-like cells promoting the differentiation of PC12 cells and forming Myelin in vitro. *Stem Cells Int.* **2015**, 328957 (2015).
67. Y. Li, Y. Sheng, J. Liang, X. Ren, Y. Cheng, Glial differentiation of human inferior turbinate-derived stem cells: A new source of cells for nerve repair. *Neuroreport* **28**, 235–241 (2017).
68. S. H. Hwang, S. Y. Kim, S. H. Park, M. Y. Choi, S. A. Back, Y. Im Kim, D. I. Sun, S. W. Kim, Osteogenic differentiation of human turbinate mesenchymal stromal cells. *Tissue Eng. Regen. Med.* **8**, 544–553 (2011).
69. S. W. Kim, J. H. Cho, M. W. Hong, J.-W. Rhie, H. R. Yoon, Induction of chondrogenic differentiation in cultured fibroblasts isolated from the inferior turbinate. *Otolaryngol. Head Neck Surg.* **139**, 143–148 (2008).
70. S. W. Hwang, S. H. Park, J. Choi, D. C. Lee, J. H. Oh, U. C. Yeo, S. W. Kim, D. I. Sun, Age-related characteristics of multipotent human nasal inferior turbinate-derived mesenchymal stem cells. *PLOS ONE* **8**, e74330 (2013).
71. S. H. Hwang, S. Y. Kim, S. H. Park, M. Y. Choi, H. W. Kang, Y.-J. Seol, J. H. Park, D.-W. Cho, O. K. Hong, J. G. Rha, S. W. Kim, Human inferior turbinate: An alternative tissue source of multipotent mesenchymal stromal cells. *Otolaryngol. Head Neck Surg.* **147**, 568–574 (2012).
72. C.-T. Kuo, J.-Y. Wang, Y.-F. Lin, A. M. Wo, B. P. C. Chen, H. Lee, Three-dimensional spheroid culture targeting versatile tissue bioassays using a PDMS-based hanging drop array. *Sci. Rep.* **7**, 4363 (2017).
73. S.-W. Yu, S.-H. Baek, R. T. Brennan, C. J. Bradley, S. K. Park, Y. S. Lee, E. J. Jun, K. J. Lookingland, E.-K. Kim, H. Lee, J. L. Goudreau, S. W. Kim, Autophagic death of adult hippocampal neural stem cells following insulin withdrawal. *Stem Cells* **26**, 2602–2610 (2008).
74. T. D. Palmer, J. Takahashi, F. H. Gage, The adult rat hippocampus contains primordial neural stem cells. *Mol. Cell. Neurosci.* **8**, 389–404 (1997).

Funding: We thank the CCRF of the DGIST for technical support. This work was supported by the National Research Foundation of Korea (NRF) funded by the Ministry of Science and ICT (no. 2017K1A1A2013237); by the Korea Evaluation Institute of Industrial Technology (KEIT) funded by the Ministry of Trade, Industry, and Energy (MOTIE) (no. 10052980); and by the DGIST MIREBraiN program. **Author contributions:** S.J. and S.K. designed and fabricated the microrobots; conducted all experiments in an in vitro, ex vivo, and in vivo environment; analyzed the data; and wrote the manuscript. S.H. characterized the hippocampal NSCs cultures, performed the differentiation and immunocytochemistry experiments, and wrote the manuscript. S.L. designed and fabricated microrobots. E.K. cultured and characterized the hTMSCs and performed the in vivo experiment. S.W.K., S.H.P., and J.H.J. provided hTMSC by isolation from human body and characterized them, and wrote the manuscript. S.Y.K. and C.M. produced the ex vivo brain model and wrote the manuscript. B.J.N. guided analysis data of the microrobot experiments and reviewed the manuscript. J.-y.K. designed and performed microrobot experiments with microorgans and the microfluidic platforms, fabricated MTs and the BoC platform, analyzed the data, and wrote the manuscript. S.-W.Y. guided analysis of the hippocampal NSC–related data and wrote the manuscript. H.C. designed the experiments, coordinated the study, and wrote the manuscript. **Competing interests:** B.J.N. is a cofounder of MagnebotiX AG. The other authors declare that they have no competing interests. **Data and materials availability:** All data needed to evaluate the conclusions in the paper are present in the paper or the Supplementary Materials. Contact J.-y.K., S.-W.Y., or H.C. for materials

Submitted 14 September 2018
Accepted 25 April 2019
Published 29 May 2019
10.1126/scirobotics.aav4317

Citation: S. Jeon, S. Kim, S. Ha, S. Lee, E. Kim, S. Y. Kim, S. H. Park, J. H. Jeon, S. W. Kim, C. Moon, B. J. Nelson, J.-y. Kim, S.-W. Yu, H. Choi, Magnetically actuated microrobots as a platform for stem cell transplantation. *Sci. Robot.* **4**, eaav4317 (2019).

Science Robotics

Magnetically actuated microrobots as a platform for stem cell transplantation

Sungwoong Jeon, Sangwon Kim, Shinwon Ha, Seungmin Lee, Eunhee Kim, So Yeun Kim, Sun Hwa Park, Jung Ho Jeon, Sung Won Kim, Cheil Moon, Bradley J. Nelson, Jin-young Kim, Seong-Woon Yu, and Hongsoo Choi

Sci. Robot. **4** (30), eaav4317. DOI: 10.1126/scirobotics.aav4317

Science Robotics (ISSN 2470-9476) is published by the American Association for the Advancement of Science. 1200 New York Avenue NW, Washington, DC 20005. The title *Science Robotics* is a registered trademark of AAAS.